Non-Intrusive Practitioner Pupil Detection for Unmodified Microscope Oculars

Wolfgang Fuhl[a,1], Thiago Santini[a,2], Carsten Reichert[b,3], Daniel Claus[b,4], Alois Herkommer[b,5], Hamed Bahmani[c,6], Katharina Rifai[c,7], Siegfried Wahl[c,8], Enkelejda Kasneci[a,9]

[a] *Perception Engineering, Eberhard-Karls-University Tübingen, Sand 14, 72076 Tübingen, Germany*
[b] *Institute of Technical Optics, University Stuttgart, Pfaffenwaldring 9, 70569 Stuttgart, Germany*
[c] *ZEISS Vision Science Lab, Röntgenweg 11, 72076 Tübingen, Germany*

Abstract

Modern microsurgery is a long and complex task requiring the surgeon to handle multiple microscope controls while performing the surgery. Eye tracking provides an additional mean of interaction for the surgeon that could be used to alleviate this situation, diminishing surgeon fatigue and surgery time, thus decreasing risks of infection and human error. In this paper, we introduce a novel algorithm for pupil detection tailored for eye images acquired through an unmodified microscope ocular. The proposed approach, the Hough transform, and six state-of-the-art pupil detection algorithms were evaluated on over 4000 hand-labeled images acquired from a digital operating microscope with a non-intrusive monitoring system for the surgeon eyes integrated. Our results show that the proposed method reaches detection rates up to 71% for an error of $\approx$ 3% w.r.t the input image diagonal; none of the state-of-the-art pupil detection algorithms performed satisfactorily. The algorithm and hand-labeled data set can be downloaded at:(on acceptance)

Keywords: pupil detection, pupil center estimation, surgical microscope

1. Introduction

Modern computer science tries to automate medical procedures to relieve medical staff from exhausting, error prone, and critical tasks, such as patient observation, support in disease classification, knowledge transfer, and process optimization. For instance, Rahimi-Gorji et al. have employed computational methods to investigate inhalation and exhlation, considering disease classification, passive patient observation, and employing inhalation as a mechanism for non-invasive medication delivery [1, 2, 3]. Such efforts alleviate the presure on an (overworked) medical workforce. Eye tracking has proved to be a tangible tool for monitoring and interaction in a multitude of fields, ranging from conspicuous applications – such as human-computer interaction [4, 5] and marketing research [6] – to less obvious ones, like inferring a subject's state of attention [7] or fatigue [8]. Whereas eye tracking is already applied in the field of microsurgery (e.g., incorporated into LASIK's[10] delivery systems to lessen the effect of patient eye movement [9]), little to no attention has been given to the user on the opposite perspective of the microscope (i.e., the surgeon). From this point of view, there is much to be gained. Throughout microsurgery, typically all of the

[1]wolfgang.fuhl@uni-tuebingen.de
[2]thiago.santini@uni-tuebingen.de
[3]reichert@ito.uni-stuttgart.de
[4]claus@ito.uni-stuttgart.de
[5]herkommer@ito.uni-stuttgart.de
[6]hamed.bahmani@uni-tuebingen.de
[7]Katharina.Rifai@zeiss.com
[8]siegfried.wahl@zeiss.com
[9]Enkelejda.Kasneci@uni-tuebingen.de
[10]Laser-assisted in situ keratomileusis

(a) Body (b) Mouth piece (c) Pedal

Figure 1: Control inputs from the Opmi Pentero 900 and 800 operating microscopes (source Carl Zeiss AG `https://www.zeiss.com`). The microscope body (a), containing the two occulars and controls to adjust the system settings. The mouth piece (b), including a control element to hand-freely steer the system. The foot pedal (c), allowing for additional control over some of the many degrees of freedoms in the system.

surgeon's extremities are busy; a modern operating microscope includes features for directional movements, zooming, focusing, and illumination, which the surgeon manages through several controls in the microscope body, foot pedal, or mouth pieces (see Fig. 1). Thus, eye tracking as an additional input method would be immensely convenient and potentially yield multiple benefits. By enabling the surgeon to move the system faster and effortlessly, fatigue and operation time are diminished. Naturally, a less fatigued surgeon is less likely to perform harmful mistakes [10, 11], and faster operation times decrease the risk of infection [12, 13]. Moreover, surgeon fatigue could also be assessed from the eye tracking data by means of pupillometric information. Additionally, the gaze information can be easily shared with other co-observers (e.g., a co-surgeon), this also eliminates the need for verbal cues (e.g., "see the nerve at 3 o'clock"), which may be misleading due to different image orientations between surgeon and co-observer [14]. Furthermore, scanpaths of expert surgeons can be integrated into educational systems, thus speeding up the learning process for students and novice surgeons [15]. It is worth noticing that any changes to the microscope that alter its current form would not only lead to an increase in manufacturing costs, but could also affect its usability, increasing the learning curve of the system and forcing experienced users to readapt. The system here proposed was designed with such issues as first-class requirements; thus, our approach not only can be applied as a plug-in device that requires no system modifications but is also based on a non-intrusive and intuitive input device, namely video-based eye-tracking.

Tracking the eyes of a microscope user differ significantly from traditional head-mounted or remote eye tracking. Remote eye trackers typically consist of a camera system placed in front of the user and provide an image containing the user's face (Fig. 2b); the localization of the eyes is then identified, and the resulting eye box (Fig. 2c) is used as input for the pupil detection algorithm. Head-mounted eye trackers place the camera system directly facing the user's eye and, thus, do not require locating eye boxes. The eye camera image (Fig. 2d) is used as input for the pupil detection algorithm. Both systems commonly employ near infrared illumination (with wavelengths ranging from 860nm to 900nm [16]) to improve the contrast between the pupil and iris. The size and placement of the microscope impedes the utilization of these traditional eye tracking approaches. Instead, an imaging device can be coupled within the microscope optics in order to obtain images from the user's eyes, resulting in images from a perspective inside the microscope eyepiece (Fig. 2a). From this perspective, the main challenge is that only a small part of the eye (and often only a small part of the pupil) are visible due to occlusion by the eyepiece. Although this issue can be attenuated by a redesign of the optical system, such a procedure is expensive and time consuming. We provide an extensive analysis of challenges arising in this scenario in Section 4.

In this work we will focus on operating microscopes as a practical and tangible use case; however, it is worth

(a) Microscope (b) Remote (c) Remote eye box (d) Head-mounted

Figure 2: Sample images from remote, head-mounted, and microscope-integrated eye tracking. Note that only a small part of the eye and pupil are visible in the microscope image (the dashed yellow line represents the contour of the eyepiece).

noticing that the proposed approach can be employed in other varieties of microscopes with similar benefits. The proposed method was compared to six state-of-the-art algorithms on 4263 images recorded using a pupil monitoring system integrated into a digital stereo microscope. Our results demonstrates that existing methods are not able to handle such images; in contrast, the proposed method performs satisfactorily, reaching a detection rate of 71.8% at a relative error of 2%.

2. Related work

Although multiple algorithms for pupil center detection exist, none is especially designed for greatly enlarged pupil recordings in which the pupil is usually only partially visible. In fact, such an input violates basic premises of some algorithms, precluding their usage. In this work, we have selected three algorithms designed for remote eye trackers and three for head-mounted eye trackers as baselines for evaluation; these were chosen based on their applicability and performance; these algorithms are described below[11].

Droege and Paulus [19] developed an algorithm which uses a bandpass filter on image pixel gradients. The gradient positions and slopes are interpreted as lines in Hessian form. Using an M-Estimator the intersection of those lines with the smallest distance to all lines is estimated and used as pupil center. **Timm and Barth** [20] also use gradients for estimating the pupil center with the difference that they inspect the angle between the vector of a possible center to the gradient position and the gradient of this point. The center position with the lowest summed up angle difference weighted by the centers intensity value is used as pupil center estimation. **George and Routray** [21] use the orientation anulus [22], vertically stronger weighted, for coarse positioning. Afterwards the gradients in a specified radius range are collected and filtered based on their angle and magnitude. The remaining gradients are median filtered and a RANSAC ellipse fit is applied for center estimation. **ExCuSe** [23] and **ElSe** [24] are based on edge selection followed by morphological filtering. The former employs an angular integral projection function [25] for coarse positioning if no reflection is expected. The latter uses a weighted blob detection if the edge based detection fails. **Starburst** [26] is based on sending out rays from a initial position, selecting intersected edge points. Based on the selected edge points a new center is estimated, and new rays are send out. This is done until convergence, and a RANSAC based ellipse fitting is applied for pupil center estimation.

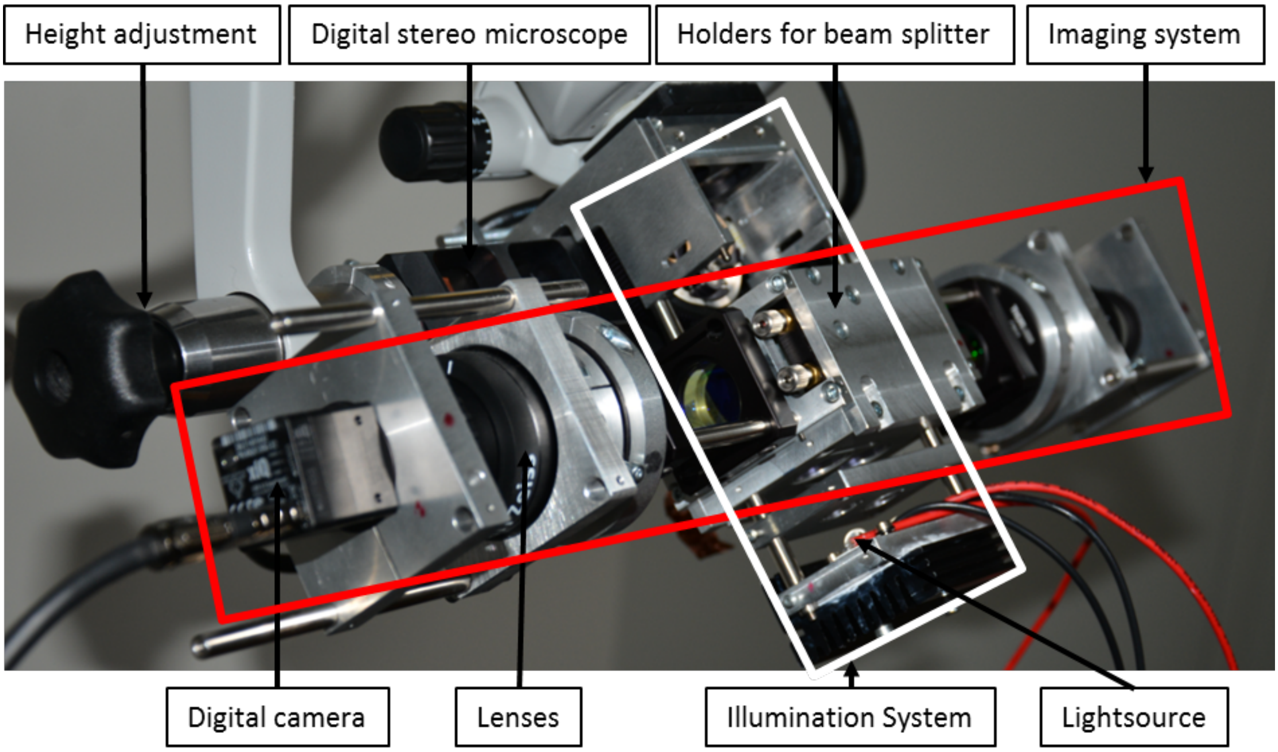

Figure 3: System imaging and illumination setup. The white box highlights the light path from the display to the oculars (from bottom to top). The beam splitters located at the intersection of the white and red boxes split the light returning from the user eyes, directing a light beam to the imaging system (red box). The cameras at the endings of the red box record capture images of the occular openings (i.e., parts of the user eyes).

3. Recording system description

The usage of an unmodified ocular for pupil detection poises the challenge of extracting the pupil image out of the light returning from the eye into the microscope. This can be accomplished by beam splitters, which direct the reflected light of the surgeons eye to the pupil monitioring system (imaging system in figure 3). This can be seen in figure 3 at the left and right border of the red box. The digital camera is the pupil monitoring system. The intersection between the white and the red box is the location of the beam splitters, which redirect the light incoming from the occular opening (light coming from the top of the white box).

We developed an illumination and imaging device, which can easily be attached to an existing digital stereo microscope, where stereoscopic images are displayed on two digital high resolution displays. Figure 3 shows the setup design of the illumination and imaging system for the pupil monitoring. We used two Vistek cameras (eco415MVGE) to monitor the eyes pupil position. The displays of the digital stereomicroscope are used as an imaging source and also as illumination source for monitoring the users pupil position. The systems accessible field of view at the eye position is limited to 4x4 mm^2 due to the eyepiece, imposing some constrains on the pupil movement range. In addition to the lateral pupil movement, the surgeon also has to move and turn his head in order to view the outermost positions of the displays. As a result, only a small portion of the pupil is visible at times due to the limited field of view during recording. Other critical parameters restricting satisfactory recordings were the high Numerical Aperture (NA) of the system at the eye location, which results in a small depth of field (DOF=0.1 mm) and, hence, a strong blurring at very small longitudinal displacement of the eye. Although a high NA was chosen

[11] A comprehensive review of pupil detection algorithms is given in [17, 18].

to increase the amount of light, this limits the depth of field; in order to alleviate this limitation, an iris diaphragm was introduced at an intermediate plane, hence relaxing positional constrains on the user eyes. With this method, a DOF of 1.4 mm could be obtained. However, this appraoch can lead to blurred and smeared images due to the reduced irradiance, which requires an increased exposure time and result in the superposition of multiple eye pupil positions within a single frame. Thus, a compromise between high DOF and sufficient irradiance was found, and a chin-rest was employed to reduce longitudinal displacements of the user's eyes.

4. Dataset and Challenges

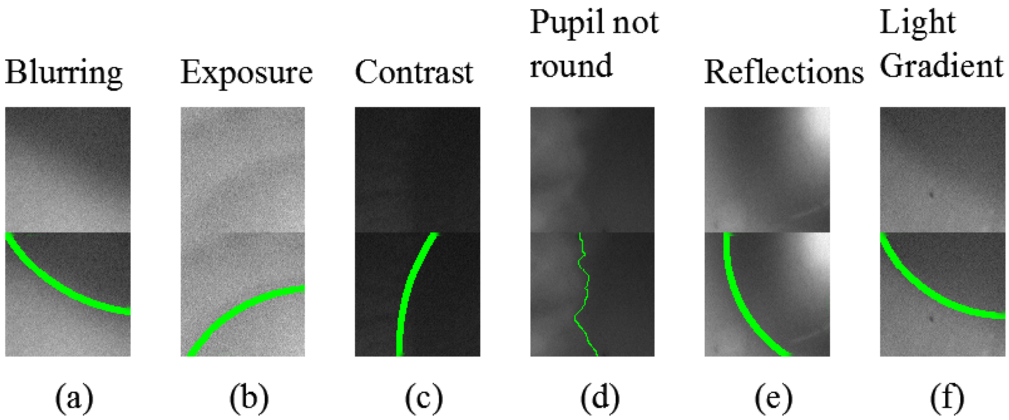

Figure 4: Challenges for pupil center detection arise in the data sets. The green line in the images below show the pupil border.

The data set images have a resolution of 512x388 pixels with pupil diameters ranging from 170 to 350 pixels. Two subjects participated in the data colletion process; for each subject, three recordings were performed in different conditions. Recordings from the first subject were assigned even identification numbers, whereas recordings from the second subject received odd ones. The size of hand-labeled images in each data set is as follows: data set I (238), data set II (971), data set III (983), data set IV (891), data set V (802) and data set VI (378). The unequal data size stems from removed images that the human annotator was not able to label manually (e.g., due to reflections covering the complete image, too low contrast, subject completely out of the focus plane). Figure 5 shows examples from all data sets; the green circle delimits the pupil ouline. As can be seen in the comparison of data set I to all the others, the lightning conditions can change heavily due to changes in the objective (i.e., screen) brightness, with the lack thereof leading to poor exposure (Fig. 4b). It is worth noticing that exposure could not be performed using infrared light because of the design of the ocular. Since the system is optimized for visible light, a low reflective glass for the visible light spectrum is employed in the ocular, which is highly reflective to infrared light; this can lead to low contrast (e.g., for data set IV: Fig. 4c). Blurred pupil outlines (e.g., data sets II and VI) can be caused by eye movements or limited focus plane through the microscope ocular (Fig. 4a), and a not round pupil contour can result even in sharp images (e.g., data set III: Fig. 4d). Objetive (a digital display emitting light with wavelengths between 390 and 700 nm) reflections on the cornea also occur often. These reflections are present in all data sets (e.g., Figure 4e). Furthermore, the reflections on the cornea, the lenses in the eyepiece, and the unbalanced screen exposure lead also to light gradients in the image as shown in Figure 4f.

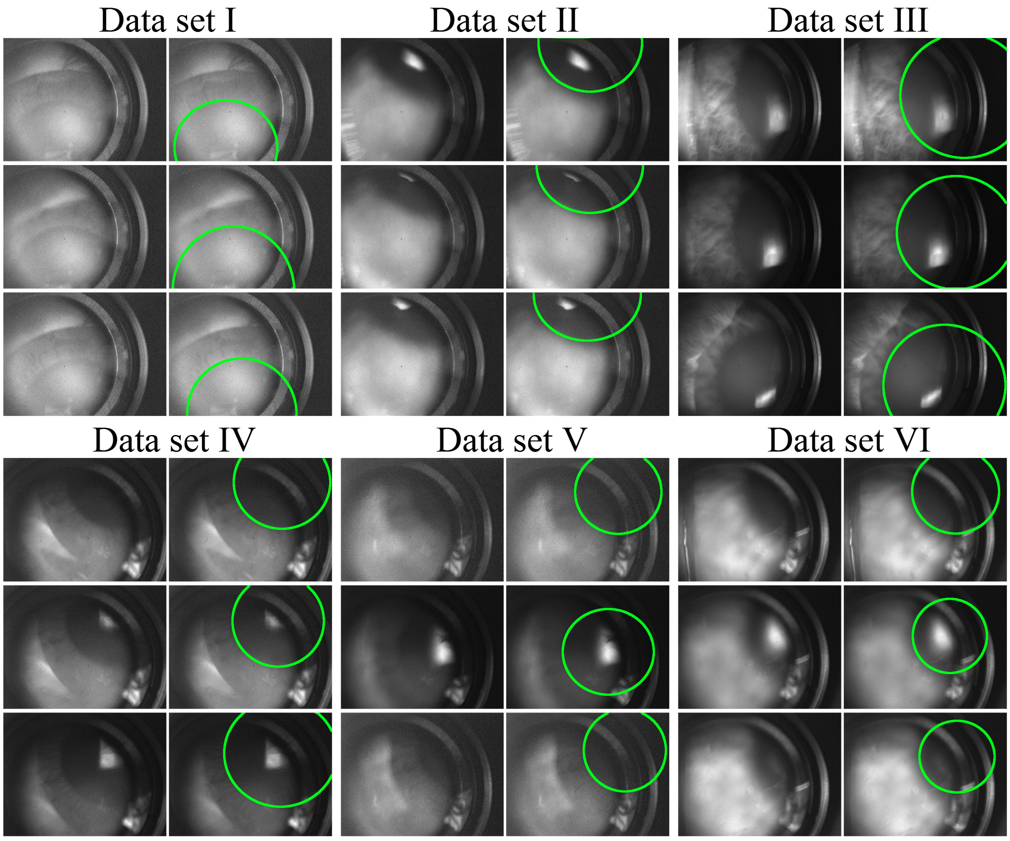

Figure 5: Collected data sets; for each data set three images are shown accompanied by the image with the hand-labeled pupil outline overlayed in green.

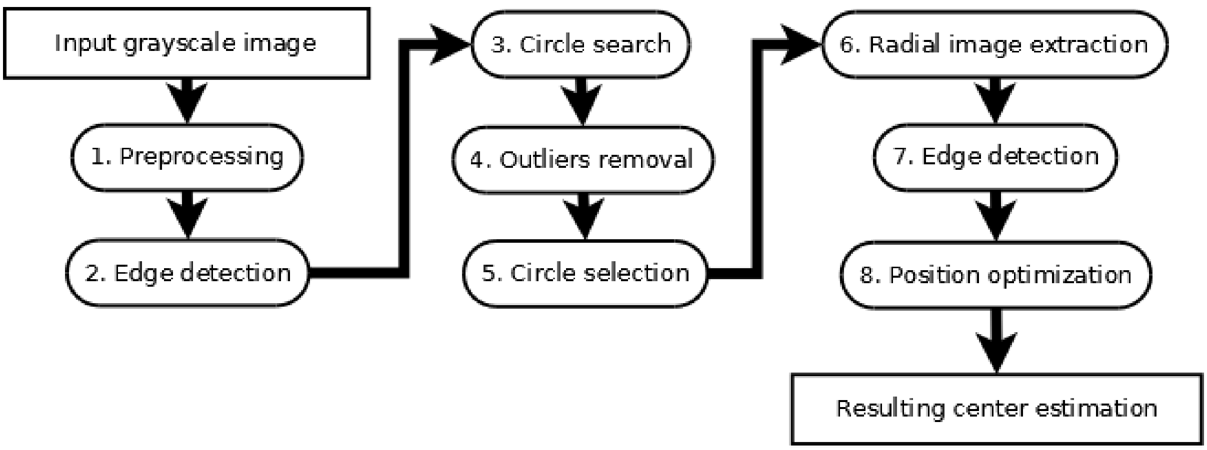

Figure 6: The algorithmic workflow for pupil center detection. Rounded boxes represent processing steps of the algorithm and squared boxes are the input and output.

5. Method

The input to the algorithm are 8-bit gray-scale images and a masking matrix for the area of interest. The workflow is shown in Fig. 6. In the following subsections, each step is described in detail.

5.1. Preprocessing

The preprocessing consists of three steps. In the first step, the image is smoothed using a Gaussian filter to reduce noise. Then the image is inverted and squared, serving as a high pass filter. Because of the high variations in the input images, the third step consists of averaging the result of the second step. This assigns larger weights to intensity values higher than the Gaussian function and is, therefore, more robust to intensity fluctuations that can origin from the high pass calculation.

In Equations (1), (2) and (3), X and Y represent image coordinates, X_0 and Y_0 are the coordinates of the center position, σ is the standard deviation. The first step represents the Gaussian convolution $I(X,Y) * Gauss(X,Y,\sigma)$, where $I(X,Y)$ is the inverted input image. The second step is described by Equation (3), in which the first step can be seem in the denominator. The operation conducted in the last step is represented by 3, in which t represents the size of the box for the averaging function.

$$Gauss(X,Y,\sigma) = \frac{1}{2\pi\sigma^2} e^{-\frac{(X-X_0)^2+(Y-Y_0)^2}{2\sigma^2}} \tag{1}$$

$$Highpass(X,Y) = \frac{1}{(1+(I(X,Y) * Gauss(X,Y,\sigma)))^2} \tag{2}$$

$$Box(X,Y,t) = \begin{cases} 0, |X-X_0| > t \\ 0, |Y-Y_0| > t \\ 1, otherwise \end{cases} \tag{3}$$

5.2. Edge detection

To extract edges, we apply a Canny operator [27] combined with a multi scale enhancement technique inspired by edge focusing as presented in [28]. First, we rescale the image shown in Fig. 7b to different scales as in [29]. Afterwards, we apply the Canny edge detector to each scale. A valid edge pixel has to be present in each scale; otherwise, it is discarded from further processing. This process is shown in Fig. 8b, where the black boxes represent

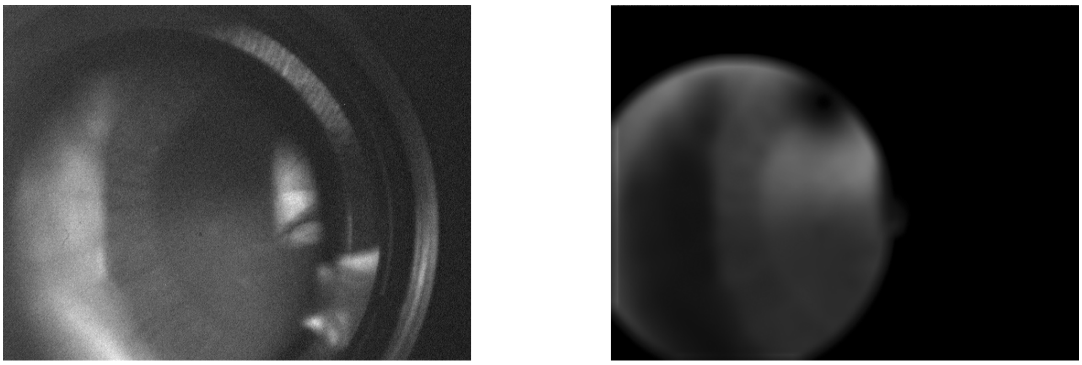

(a) (b)

Figure 7: (a) shows the input grayscale image (recorded from the imaging system in figure 3). In (b) the image after preprocessing is shown.

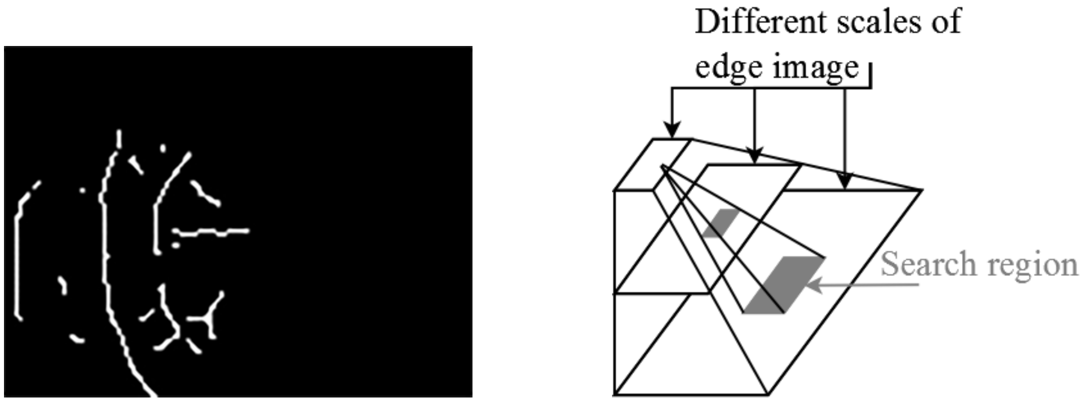

(a) (b)

Figure 8: (a) shows the result of the edge detection (combination of all results from the pyramid in (b)). (b) shows the pyramid of edge images, where those are represented as black boxes. The dark gray boxes represent search regions for edge filtering in a higher resolution scale, meaning that edges have to be present in all gray boxes to be valid.

the different scales of the edge image, and the dark gray boxes represent search regions in higher scales to decide if a edge pixel is valid or not.

$$Edge(e) = \begin{cases} 1, \forall i \exists a \in S_i, a = e \\ 0, otherwise \end{cases} \tag{4}$$

In Equation (4), S_i represents the edge image in scale i and e the extracted edge pixel. The result of this step for Fig. 7b can be seen in Figure 8a.

5.3. Circle search

To estimate the pupil center, we first search for all possible circles since we assume the pupil to be round and not elliptical. To accomplish this, we inspect each line and, for all possible pairs of line points, search for a possible circle segment height outgoing from the center of both selected points. The segment height is searched orthogonally to the vector between both points.

$$Radius(tendon, h) = \frac{4 * h^2 + tendon^2}{8 * h} \tag{5}$$

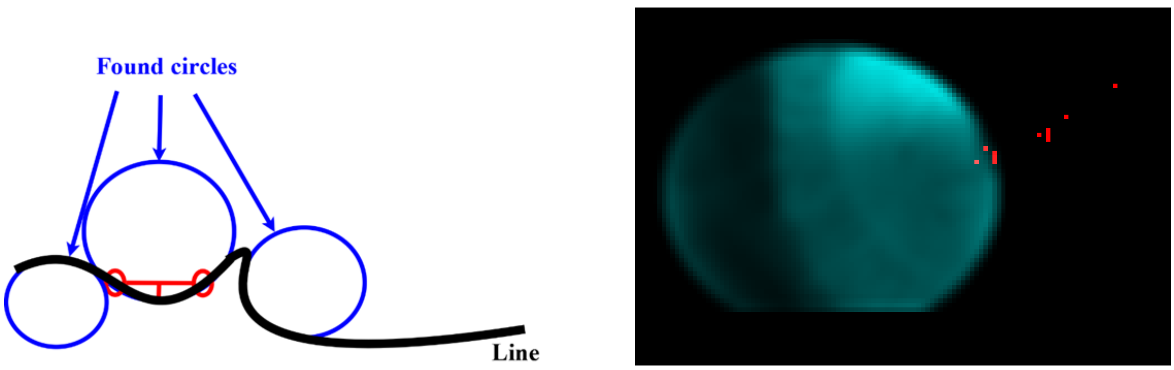

(a) (b)

Figure 9: (a) shows the workflow of the circle search. The black line represents edge pixels while the red circles represent two selected edge pixels. The red lines show an exemplary circle tendon and circle segment height which are used for circle radius calculation (blue circles). In (b), valid circle votes are drawn as red dots (those are the centers of all valid blue circles).

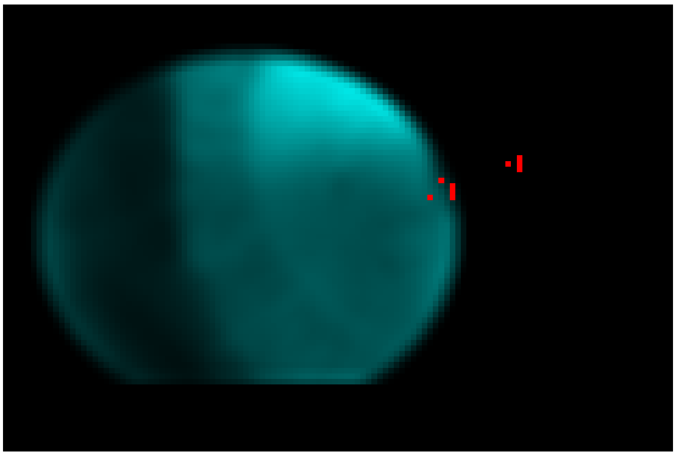

Figure 10: All remaining pupil center candidates (red dots) after outliers removal.

Equation (5) represents the circle radius calculation based on tendon and segment height. *tendon* is the length of the tendon of the circle segment and h the height of this segment (red lines in Fig. 9a). All radii that are too high or too low to be a possible pupil radius are discarded. Found valid pupil centers are shown in Fig. 9b as red dots.

5.4. Outliers removal

Outliers detection is done under the assumption that most of all votes belonging to a line are valid and that the variation between those votes follows a normal distribution. Therefore, the outliers removal is done based on the 95% quantile on the standard deviation of all votes of a line. Fig. 10 shows the remaining votes from Fig. 9b after outlier removal.

$$\tau = \frac{q_{0.95} * (n-1)}{\sqrt{n} * \sqrt{(n-2) * (q_{0.95}^2)}} \tag{6}$$

$$\phi = std(centers) * \tau \tag{7}$$

$$Outlier(i) = \begin{cases} 1, |centers(i) - mean(centers)| > \phi \\ 0, else \end{cases} \tag{8}$$

Equations (6), (7) and (8) describe this iterative process. After each outliers removal step, the parameters τ and ϕ have to be recalculated. In Equation (6), $q_{0.95}$ represents the 95% quantile, whereas n represents the number of found centers for a line. In Equations (7) and (8), *std* represents the standard deviation and i the index of a found pupil center. This step can also remove correct center estimates if an image is blurred and the edges are inaccurate. Therefore, we used an upper bound of votes per line for which no outlier selection has to be performed (in our implementation we used 6 as upper bound).

5.5. Circle selection

To select the pupil center, all remaining votes are inspected in an inverse manner. Outgoing from the estimated center and the calculated radius, the edge value is recalculated. The idea behind this step is that non-connected edges can vote for the same center. The gray circular ring in Fig. 11 represents the area that is inspected for one center vote. In this area, the difference between the closest and the furthest part is calculated and summed up. This

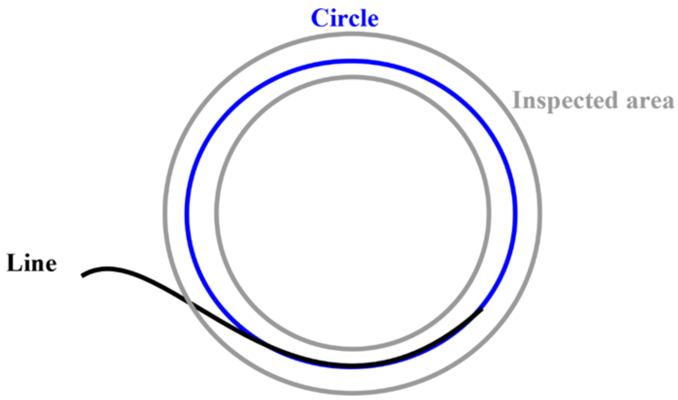

Figure 11: Recalculation of the edge value outgoing from a possible pupil center. The black line represents a found edge in Step 2. The gray area is the inspected area for edge value calculation and the blue line represents the calculated circle.

is only done if an edge pixel is present. The closest part is defined as the intensity values before this edge pixel, and the furthest part is defined by the intensity values after the edge pixel outgoing from the center.

$$RI(c,\alpha,r) = I(c_x + cos(\alpha) * r, c_y + sin(\alpha) * r) \tag{9}$$

$$V(c,\alpha) = \begin{cases} \frac{1}{e-1-r_{min}} \sum_{i=r_{min}}^{e-1} RI(c,\alpha,i) - \\ \frac{1}{r_{max}-e+1} \sum_{i=e+1}^{r_{max}} RI(c,\alpha,i), \\ \exists e \in RI(c,\alpha,r_{min} : r_{max}) \\ \\ 0, else \end{cases} \tag{10}$$

$$EV(c) = \frac{1}{2*\pi} \sum_{i=0}^{2*\pi} V(c,i) \tag{11}$$

Equation (9) describes the transformation from a center point c to its radial intensity value specified by the radius r and the angle α. In Equation (10), these values are used to calculate the intensity difference between two areas in Figure 11: 1) the area between the inner ring (given by r_{min}) and the the edge pixel e ($Line$) and 2) the area between e and the outer ring (given by r_{max}). Equation (11) uses this function to calculate the complete intensity difference of the circular ring. The center with the highest edge value is selected as pupil center. To correct for small pupil center jitter, the found position is stabilized in the subsequent steps.

5.6. Radial image extraction

The first step for position stabilization is the extraction of a radial image using Equation (9). The selected image lines are shown as white lines in Fig. 12a. The resulting radial image is shown in Fig. 12b. The height of the image shown in Fig. 12b is the length of the white lines shown in Fig. 12a and represents therefore the radius. For each angle, one line is added to Fig. 12b; thus, the widths represent the angles.

5.7. Edge detection

For edge detection in the radial image, only vertical intensity differences have to be calculated. Therefore, the image is calculated by subtracting the intensity value of the inspected pixel from the subsequent value (vertically).

$$ERI(X,Y) = |I(X,Y) - I(X,Y+1)| \tag{12}$$

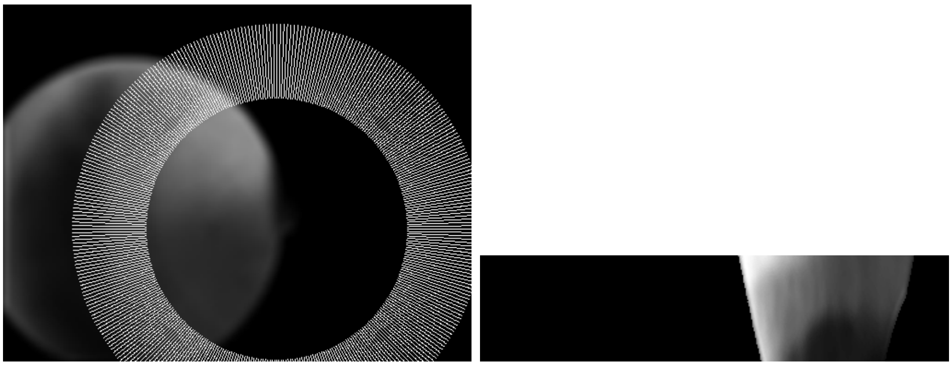

(a) (b)

Figure 12: In (a), the white lines represent the extracted image parts. (b) is the resulting image segment where the height is the radius, and the widths are the different angles. Therefore lining up the white lines in (a) result in (b).

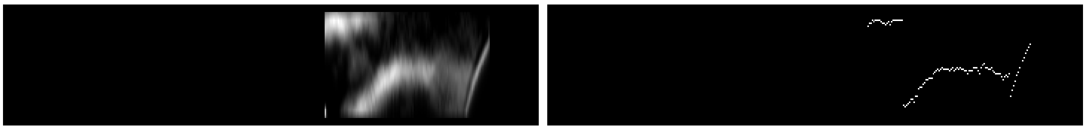

(a) (b)

Figure 13: In (a) the magnitude image of the radial image is shown, which is used for edge detection (intensity differences calculated on figure 12(b)). (b) shows the found maximal responses as white dots, which are the detected edges.

In Equation (12), this calculation is shown with X and Y representing the coordinates, and $I(X, Y)$ the intensity value in the radial image. The result is shown in Fig. 13a. For each vertical line in this image, the maximum is searched and marked as a white dot in Fig. 13b. These white pixels are the maximal votes for each angle, whereas each white dot represent a radius.

5.8. Position optimization

All of the maximas found in the edge detection step are collected in a histogram of all found radii (Fig. 14). In this histogram the smallest segment with at least one third of all radi is searched. All edge values in the selected segment are collected, and a least squares circle fit is applied. The resulting circle center is used as pupil center estimation.

$$a * X + b * Y + c = -(X^2 + Y^2) \tag{13}$$

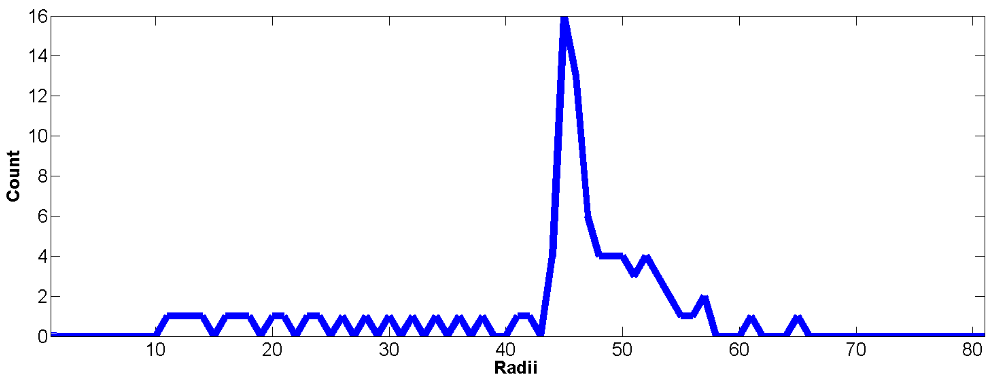

Figure 14: All found radii (white dots in Fig. 13b) as histogram (downscaled radii). Where the x axis corresponds to the radii and the y axis the amount of occurrences of this radii.

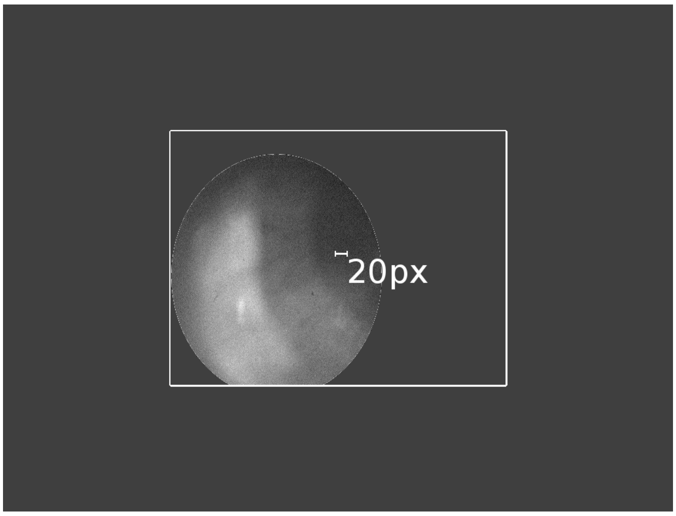

Figure 15: Input to the compared algorithms. The gray area is the mean value of the image part, and the white box ist the original image size. The small white line on the pupil is exactly 20 pixels long. This distance is the vertical dashed green line in the evaluation plots from Fig. 16.

Equation (13) shows the linear equation system that has to be solved, where X and Y represent all collected circle border coordinates. The center of the circle is given by $(-\frac{a}{2}, -\frac{b}{2})$, and $sqrt(\frac{a^2+b^2}{4} - c)$ is the radius.

6. Evaluation

We evaluated our approach against three state-of-the-art remote pupil center detection algorithms, three head-mounted ones, and the Hough transform. As evalution metric, we used the relative error given by the euclidean distance from the estimate to the labeled pupil center divided by the maximal error. As maximal error we used the image diagonal multiplied by two because it is possible that the pupil center is outside of the image. We tried to adapt the other algorithms to be able to detect pupil centers in these microscope images. First, we gave them the same image area using the area of interest masking matrix and filled the rest of the image with the mean value of this area. Second, we increased the image by adding the half of the image size on every side of the image (see Fig. 15) and filled it again with the mean value. This is done because the algorithms ElSe [24], Timm [20], and Starburst [26] assume the pupil center to be inside of the image. The last adaption was done based on the parameter setting for the best possible result. For evaluation of the Hough transform, we selected always the center vote with the highest magnitude, which delivered the best results.

The results are shown in Fig. 16 for each data set individually. Data set III (Fig. 16c) has the best results due to the quality of its images; as can be seem in Fig. 5, this data set has the sharpest images and therefore the best quality – even if the contrast is low for some images. The images from data set I also have a good focus but are very noisy, which has a high impact on the accuracy (Fig. 16a). For data set IV, the main impact on the accuracy is that only a small part of the pupil is visible. The light gradients and also the perspective distortion at the border of the lens leads to inaccurate and wrong located edges.

7. Conclusions

We proposed an novel algorithm for pupil center detection based on high resolution pupil images where the recording area is very limited, improving the state-of-the-art in regards to robustness and accuracy. Additionally, we detail the problems occurring in these novel eye tracking setup where the surgeons pupil is recorded through

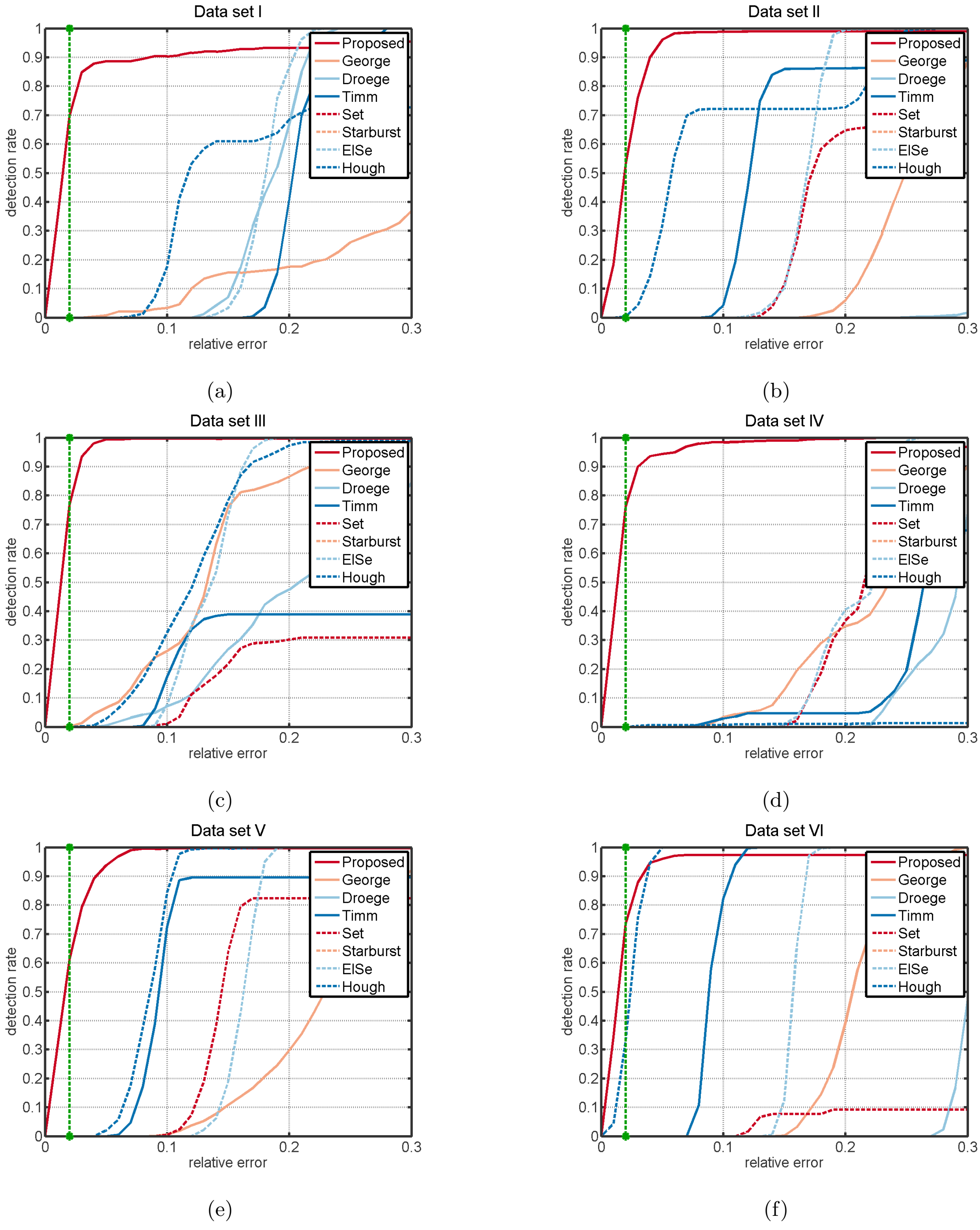

Figure 16: Results for all evaluated algorithms on the microscope data sets. The bottom axes shows the euclidean pixel distance relative to the hand labeled position divided by the maximal error, and the left axes show the percentage of correct detected pupil centers. The vertical green dashed line corresponds to an error of 20 pixels. For reference, the relation of 20 pixels to the image is shown in Fig. 15.

an unmodified microscope ocular. The comparison to the state-of-the-art algorithms from other recording setups is shown to evaluate other approaches based on edge detection, gradient direction, and thresholding with circumferential estimation. Additionally we propose a setup for pupil recording, for which the ocular or other parts in contact with the user, do not have to be changed. We will provide the MATLAB implementation and all hand labeled images (more than 4000) to support further research in this area.

References

[1] M. Rahimi-Gorji, O. Pourmehran, M. Gorji-Bandpy, T. Gorji, Cfd simulation of airflow behavior and particle transport and deposition in different breathing conditions through the realistic model of human airways, Journal of Molecular Liquids 209 (2015) 121–133.

[2] M. Rahimi-Gorji, T. B. Gorji, M. Gorji-Bandpy, Details of regional particle deposition and airflow structures in a realistic model of human tracheobronchial airways: two-phase flow simulation, Computers in biology and medicine 74 (2016) 1–17.

[3] O. Pourmehran, M. Rahimi-Gorji, M. Gorji-Bandpy, T. Gorji, Simulation of magnetic drug targeting through tracheobronchial airways in the presence of an external non-uniform magnetic field using lagrangian magnetic particle tracking, Journal of Magnetism and Magnetic Materials 393 (2015) 380–393.

[4] D. S. Best, A. T. Duchowski, A rotary dial for gaze-based pin entry, in: ETRA, ACM, 2016, pp. 69–76.

[5] M. Vidal, A. Bulling, H. Gellersen, Pursuits: spontaneous interaction with displays based on smooth pursuit eye movement and moving targets, in: UbiComp, ACM, 2013, pp. 439–448.

[6] G. Hervet, K. Guérard, S. Tremblay, M. S. Chtourou, Is banner blindness genuine? eye tracking internet text advertising, APPL COGNITIVE PSYCH 25 (5).

[7] C. Braunagel, E. Kasneci, W. Stolzmann, W. Rosenstiel, Driver-activity recognition in the context of conditionally autonomous driving, in: IEEE Trans. Intell. Transp. Syst., 2015.

[8] L. M. Bergasa, J. Nuevo, M. A. Sotelo, R. Barea, M. E. Lopez, Real-time system for monitoring driver vigilance, IEEE Transactions on Intelligent Transportation Systems 7 (1) (2006) 63–77. doi:10.1109/TITS.2006.869598.

[9] N. M. Taylor, R. H. Eikelboom, P. P. Van Sarloos, P. G. Reid, Determining the accuracy of an eye tracking system for laser refractive surgery, Journal of Refractive Surgery 16 (5) (2000) S643–S646.

[10] M. Uhrich, R. Underwood, J. Standeven, N. Soper, J. Engsberg, Assessment of fatigue, monitor placement, and surgical experience during simulated laparoscopic surgery, Surgical endoscopy 16 (4) (2002) 635–639.

[11] C. Payne, Tired eyes from microsurgeryit's blinking obvious!, Journal of reconstructive microsurgery 29 (01) (2013) 067–068.

[12] A. A. den Broeder, M. C. Creemers, J. Fransen, E. de Jong, D.-J. R. de Rooij, A. Wymenga, M. de Waal-Malefijt, F. H. van den Hoogen, Risk factors for surgical site infections and other complications in elective surgery in patients with rheumatoid arthritis with special attention for anti-tumor necrosis factor: a large retrospective study., The Journal of rheumatology 34 (4) (2007) 689–695.

[13] D. L. Edmonston, G. D. Foulkes, Infection rate and risk factor analysis in an orthopaedic ambulatory surgical center., JSOA 19 (3) (2009) 174–176.

[14] F. Schulze, How the humble stereomicroscope found its way into modern surgery: The zeiss operating microscope, Micscape Magazine.

[15] E. K. T.C. Kuebler, S. Eivazi, Automated visual scanpath analysis reveals the expertise level of microneurosurgeons, in: MICCAI15 Workshop, 2015.

[16] Z. Zhu, K. Fujimura, Q. Ji, Real-time eye detection and tracking under various light conditions, in: ETRA, ACM, 2002, pp. 139–144.

[17] W. Fuhl, M. Tonsen, A. Bulling, E. Kasneci, Pupil detection for head-mounted eye tracking in the wild: an evaluation of the state of the art, MVA (2016) 1–14.

[18] W. Fuhl, D. Geisler, T. Santini, W. Rosenstiel, E. Kasneci, Evaluation of state-of-the-art pupil detection algorithms on remote eye images, in: PETMEI, 2016.

[19] D. Droege, D. Paulus, Pupil center detection in low resolution images, in: ETRA, ACM, 2010, pp. 169–172.

[20] F. Timm, E. Barth, Accurate eye centre localisation by means of gradients., VISAPP 11 (2011) 125–130.

[21] A. George, A. Routray, Fast and accurate algorithm for eye localization for gaze tracking in low resolution images, arXiv preprint arXiv:1605.05272.

[22] T. J. Atherton, D. J. Kerbyson, Size invariant circle detection, Image and Vision computing 17 (11) (1999) 795–803.

[23] W. Fuhl, T. Kübler, K. Sippel, W. Rosenstiel, E. Kasneci, ExCuSe: Robust Pupil Detection in Real-World Scenarios, in: CAIP, Springer, 2015, pp. 39–51.

[24] W. Fuhl, T. C. Santini, T. Kübler, E. Kasneci, Else: Ellipse selection for robust pupil detection in real-world environments, ETRA '16, ACM, 2016.

[25] G. J. Mohammed, B. R. Hong, A. A. Jarjes, Accurate pupil features extraction based on new projection function, Computing and Informatics 29 (4).

[26] D. Li, D. Winfield, D. J. Parkhurst, Starburst: A hybrid algorithm for video-based eye tracking combining feature-based and model-based approaches, in: CVPR-Workshops IEEE Computer Society Conference on, IEEE, 2005, pp. 79–79.

[27] J. Canny, A computational approach to edge detection, Pattern Analysis and Machine Intelligence, IEEE Transactions on (6) (1986) 679–698.

[28] F. Bergholm, Edge focusing, Pattern Analysis and Machine Intelligence, IEEE Transactions on (6) (1987) 726–741.

[29] C. E. Duchon, Lanczos filtering in one and two dimensions, Journal of Applied Meteorology 18 (8) (1979) 1016–1022.